Dalton Transactions

ROYAL SOCIETY OF CHEMISTRY

PAPER

View Article Online
View Journal | View Issue

Check for updates

Cite this: *Dalton Trans.*, 2024, **53**, 8969

Magnetic properties and magnetocaloric effect of Ln = Dy, Tb carborane-based metal–organic frameworks†

Zhen Li, [a,b] Ana Arauzo, [c] José Giner Planas *[a] and Elena Bartolomé *[a]

Received 1st March 2024,
Accepted 12th April 2024

DOI: 10.1039/d4dt00626g

rsc.li/dalton

We present the synthesis and magneto-thermal properties of carborane-based lanthanide metal–organic frameworks (MOFs) with the formula {[(Ln)$_3$(*m*CB-L)$_4$(NO$_3$)(DMF)$_n$]·Solv}, where Ln = Dy or Tb, characterized by dc and ac susceptibility, X-ray absorption spectroscopy (XAS), X-ray magnetic circular dichroism (XMCD) and heat capacity measurements. The MOF structure is formed by polymeric 1D chains of Ln ions with three different coordination environments (Ln1, Ln2, Ln3) running along the *b*-axis, linked by carborane-based linkers thus to provide a 3D structure. Static magnetic measurements reveal that these MOFs behave at low temperature as a system of S^* = 1/2 Ising spins, weakly interacting ferromagnetically along the 1D polymeric chain (J^*/k_B = +0.45 K (+0.5 K) interaction constant estimated for Dy-MOF (Tb-MOF)) and coupled to Ln ions in adjacent chains through dipolar antiferromagnetic interactions. The Dy MOF exhibits slow relaxation of magnetization through a thermally activated process, transitioning to quantum tunneling of the magnetization at low temperatures, while both compounds exhibit field-induced relaxation through a very slow, direct process. The maximum magnetic entropy changes ($-\Delta S_m^{max}$) for an applied magnetic field change of 2-0 T are 5.71 J kg^{-1} K^{-1} and 4.78 J kg^{-1} K^{-1}, for Dy and Tb MOFs, respectively, while the magnetocaloric effect (MCE) peak for both occurs at $T \sim 1.6$ K, approximately double that for the Gd counterpart.

1. Introduction

Metal–organic frameworks (MOFs) have emerged as a transformative class of crystalline materials, owing to their intriguing porous architecture[1–3] and application potential in catalysis,[4] gas storage[5] and separation, magnetism,[6–8] sensors,[9] *etc*. Chemical design enables the creation of diverse MOF architectures, incorporating various functionalities by carefully selecting the functional nodes, organic linkages, or species inside the pores.

In particular, MOFs coordinating lanthanide ions (Ln-MOFs) exhibit unique optical, electronic, and magnetic properties derived from 4f electrons, making them attractive for applications in luminescence,[10,11] anticounterfeiting,[12] sensors,[13–15] switching,[16] thermometry,[17] magnetic refrigeration,[18–22] conductive MOFs[23] and information storage and processing,[24,25] among others.

Indeed, trivalent Ln(III) ions favor outstanding luminescence features like a large Stokes shift, high purity of colours and considerable quantum yields, especially in Tb(III) and Eu(III) ions.[12,26–28] In addition, the 4f orbitals of Ln(III) ions provide a significant magnetic moment and intrinsic anisotropy. Thus, they are good candidates for the construction of single-molecule magnets (SMMs), showcasing magnetic stability and quantum-tunneling effects.[29–31] Recent advances have shown the possibility to produce single-ion magnets (SIMs) with huge thermal activation energies close to 2000 K[32] and open hysteresis loops above the liquid nitrogen temperature,[33] using Dy(III) in an adequate coordination environment. In parallel, Ln(III) ions are being considered to encode molecular qubits,[34] offering attractive advantages for quantum computing, such as the possibility to encode multiple qubits in one sole ion,[35,36] and enlarge the quantum basis states by coupling the electronic spin with the nuclear spin.[37] The latter approach was for instance used to demonstrate the Grover algorithm in a $TbPc_2$ molecule.[38]

Therefore, Ln-MOFs represent an attractive possibility both for the preparation of ultra-high-density information storage devices[39] and the construction of spatially ordered qubit

[a]*Institut de Ciència de Materials de Barcelona (ICMAB-CSIC), Campus UAB, 08193 Bellaterra, Spain. E-mail: ebartolome@icmab.es, jginerplanas@icmab.es*
[b]*Shandong Provincial Key Laboratory of Monocrystalline Silicon Semiconductor Materials and Technology, College of Chemistry and Chemical Engineering, Dezhou University, Dezhou 253023, China*
[c]*Instituto de Nanociencia y Materiales de Aragón (INMA), Departamento de Física de la Materia Condensada, CSIC-Universidad de Zaragoza, Zaragoza 50009, Spain*

†Electronic supplementary information (ESI) available: S1: Structural characterization: supplementary figures; S2: magnetization field-dependence modeling; S3: corrected sum rules for lanthanide Ln^{3+} ions. See DOI: https://doi.org/10.1039/d4dt00626g

arrays, or "quMOFs",[40,41] for quantum computing technologies. Lanthanide SIM-MOFs constitute also an ideal benchmark to study dynamic spin magnetic relaxation, depending on the relative importance of the ions' anisotropy compared to interactions, regulated by the structure topology and linkers.[42] Achieving high-energy barriers in MOF systems remains challenging, though, due to the difficulty in preserving strong uniaxial magnetic anisotropy and controlling the easy-axis alignment of the spin carriers throughout the framework. Consequently, compared to the widespread reporting of isolated Ln-SIMs, there exist relatively few Ln-MOFs, predominantly based on Dy(III), exhibiting slow magnetic relaxation properties,[14,43–49] and the energy barriers in these systems remain modest (at most 417 K (ref. 16)).

In addition, Ln-MOFs are well suited for crafting materials with the magnetocaloric effect (MCE), for use in ultra-low temperature cooling.[18–21] Although most complexes investigated for magnetocalorics contain Gd^{3+}, because its large S = 7/2 and negligible magnetic anisotropy allow achieving the highest maximum entropy changes (typically for temperatures <2 K and applied magnetic fields >5 T),[22] some proposals advocate the use of anisotropic lanthanide ions to optimize the MCE performance for lower field changes, achievable by permanent magnets,[50] and high temperatures above 4 K.[51–53] Additionally, some interesting MOFs for MCE have been reported using [Ln_6] clusters (Ln = Gd, Dy),[54] or 4f clusters separated by 3d centres.[55]

All in all, Ln-MOFs offer immense potential for designing multifunctional materials incorporating several properties, such as magnetism combined with MCE, luminescence,[26,27,56] proton conductivity,[57,58] *etc*.

Despite the enormous interest, Ln-MOFs are relatively scarcer than their transition metal counterparts. This is because typically Ln(III) ions exhibit high coordination numbers with distorted symmetries which bring flexibility to the coordination network, making the prediction of structures more challenging. In order to build stable and efficiently functionalized MOFs, the choice of appropriate organic linkers is a key part of the framework design. Considering the diversity of the coordination modes and the high affinity between the O atom and Ln(III) ions, carboxylates have been the most popular type of spacer employed for the assembly of Ln-MOFs.[59–61] Still, the design and synthesis of new Ln-MOFs with alternative linkers is a promising endeavor, as it unlocks heightened tunability, substantially expanding their range of applications.[62]

In the last few years, we have demonstrated the efficacy of carborane-based linkers to synthesize a variety of functional MOFs.[12,63–65,66–73] Icosahedral carboranes are a class of commercially available and exceptionally stable boron-rich clusters,[74–76] possessing an unusual electronic structure, which is often highlighted by considering carboranes as inorganic 3D "aromatic" analogs of arenes.[74–76] They have high hydrophobicity,[77–83] allowing the preparation of water-stable MOFs.[12,64,65,67,71]

Recently, we reported the successful synthesis and optical properties of {[$(Ln)_3$(*m*CB-L)$_4$(NO_3)(DMF)$_n$]·Solv} (Ln = Eu, Tb, Eu/Tb),[12] using the carborane linker *m*CB-L = 1,7-di(4-carboxyphenyl)-1,7-dicarba-*closo*-dodecaborane. Moreover, we demonstrated the possibility of synthesizing multi-metallic MOFs incorporating up to eight different sized rare-earth cations,[66] leveraging the steric bulkiness and acidity of the *m*CB-L ligand. This milestone opens the way for the development of multifunctional multi-Ln MOF materials with tailored properties.

Herein, we present the magneto-thermal properties of two homonuclear MOFs of this family, {[$(Ln)_3$(*m*CB-L)$_4$(NO_3)(DMF)$_n$]·Solv}, incorporating Ln = Dy or Tb. These two lanthanides have been selected to compare the magnetic properties of two isostructural MOFs based on a Kramers ion (Dy, $^6H_{15/2}$, S = 5/2, L = 5, J = 15/2) and a non-Kramers ion (Tb, $^7F_6$, S = 3, L = 3, J = 6). The magnetic and thermal properties have been characterized by combining dc and ac magnetometry, X-ray absorption spectroscopy (XAS), X-ray magnetic circular dichroism (XMCD), and heat capacity techniques.

2. Experimental

Synthesis

All chemicals were of reagent-grade quality. They were purchased from commercial sources and used as received. The 1,7-Di(4-carboxyphenyl)-1,7-dicarba-*closo*-dodecaborane ligand (*m*CB-H_2L) was synthesized according to the literature procedure.[84] Synthesis of {[$(Ln)_3$(*m*CB-L)$_4$(NO_3)(DMF)$_n$]·Solv} (***m*CB-Ln**, where **Ln** = **Dy** or **Tb**) was performed as previously described.[12,66] In a typical preparation, *m*CB-L (0.03 mmol) and Ln(NO_3)$_3$ (0.02 mmol; Ln = Dy or Tb) were added to a mixture of DMF (0.5 mL)/methanol (1.5 mL)/H_2O (0.3 mL) and sonicated until complete dissolution of all reagents. The above mixture was transferred to an 8-dram vial and heated at 95 °C in an oven for 48 h. Needle-like white crystals were collected and washed with DMF.

Basic characterization

Powder X-ray diffraction (PXRD) was recorded at room temperature on a Siemens D-5000 diffractometer with Cu Kα radiation (λ = 1.5418 Å). Thermogravimetric analysis (TGA) was performed in N_2, on an nSTA 449 F1 Jupiter instrument (heating rate: 10 °C min^{-1}; temperature range: 25 to 800 °C).

Magnetometry

The magnetization and the dc and ac susceptibility of powdered samples were measured, above 1.8 K, using a Quantum Design superconducting quantum interference device (SQUID) magnetometer. Ac measurements were performed at an excitation field of 4 Oe, at temperatures between 1.8 K and 8.0 K, under dc fields between 0 and 3 T, while sweeping the frequency between 0.1 and 1000 Hz. Additional ac susceptibility measurements in the 10–10 000 Hz range were carried out in a Quantum Design PPMS. Measurements on powdered samples were performed with the addition of Daphne oil, introduced to fix the grains at low temperatures.

XAS and XMCD

X-ray absorption spectroscopy (XAS) and X-ray magnetic circular dichroism (XMCD) experiments across the $M_{4,5}$ edges of Dy and Tb were performed at BOREAS beamline in ALBA synchrotron. The powdered samples were crushed on an indium foil and placed at the tip of a cold finger. Measurements were performed at 3.4 K ± 0.5 K, in total electron yield (TEY) detection mode, with a 90% circularly polarized light. The XMCD ($\mu^- - \mu^+$) and XAS ($\mu^+ + \mu^-/2$) spectra at 6 T were determined from eight X-ray absorption spectra measured under right-handed (μ^+) and left-handed (μ^-) circular polarizations. XMCD(H) cycles were performed by following the resonant M_5 peak while sweeping the magnetic field between 6 T and −6 T at a rate of 2 T min^{-1}.

Heat capacity

Heat capacity as a function of temperature was measured between 0.3 and 100 K at different applied fields between 0 and 3 T on a pressed powder pellet fixed with Apiezon N grease, using a Quantum Design PPMS equipped with a ^{3}He refrigerator.

3. Results

Structural characterization

The single-crystal structure of {[(Tb)$_3$(*m*CB-L)$_4$(NO$_3$)(DMF)$_n$]·Solv} (***m*CB-Tb**) was previously determined by single-crystal X-ray diffraction (SCXRD).[12] The secondary building unit (SBU) of this MOF is composed of three non-equivalent crystallographic terbium atoms, Tb(1) and Tb(3) being eight-coordinated, while Tb(2) is seven-coordinated (Fig. 1a). The varied coordination around the three crystallographic independent Ln atoms results in three different Tb–Tb metal distances (Tb1–Tb2 4.5830(8), Tb2–Tb3 5.2550(7) and Tb1–Tb3 4.6398(7) Å). The Tb–O bond distances are in the range 2.272(10)–2.906(10) Å. These Tb cations are capped by bridging, chelate bridging or by chelating *m*CB-L, and chelating NO_3^- and DMF molecules forming 1D chains running along the *b*-axis, that are further connected by the ditopic *m*CB-L ligand and thus provide the observed 3D structure (Fig. 1b and c). Two Tb inter-chain distances can be found in the structure (11.0 and 17.4 Å; see Fig. 1b and c). Powder XRD measurements reveal that ***m*CB-Dy** is isostructural to ***m*CB-Tb** (Fig. S1†) and confirm that these single-metal ***m*CB-Ln** materials display the same crystal structure.

1D channels can be observed along the same direction as the 1D-Tb chains that can accommodate guest molecules (Fig. 1c). Thermogravimetric analysis indicates that both materials undergo loss of the solvent (coordinated to metal sites and/or distributed in the pores) in the range 200–350 °C and decomposition of the framework above 450 °C (Fig. S2†). Following thermal activation (elimination of solvent in the voids through high vacuum thermal treatment), sorption measurements indicated that ***m*CB-Dy** and ***m*CB-Tb** compounds are non-porous to N_2 but porous to CO_2, with Dubini–Radushkevich surface areas of 196 and 331 m^2 g^{-1}, respectively

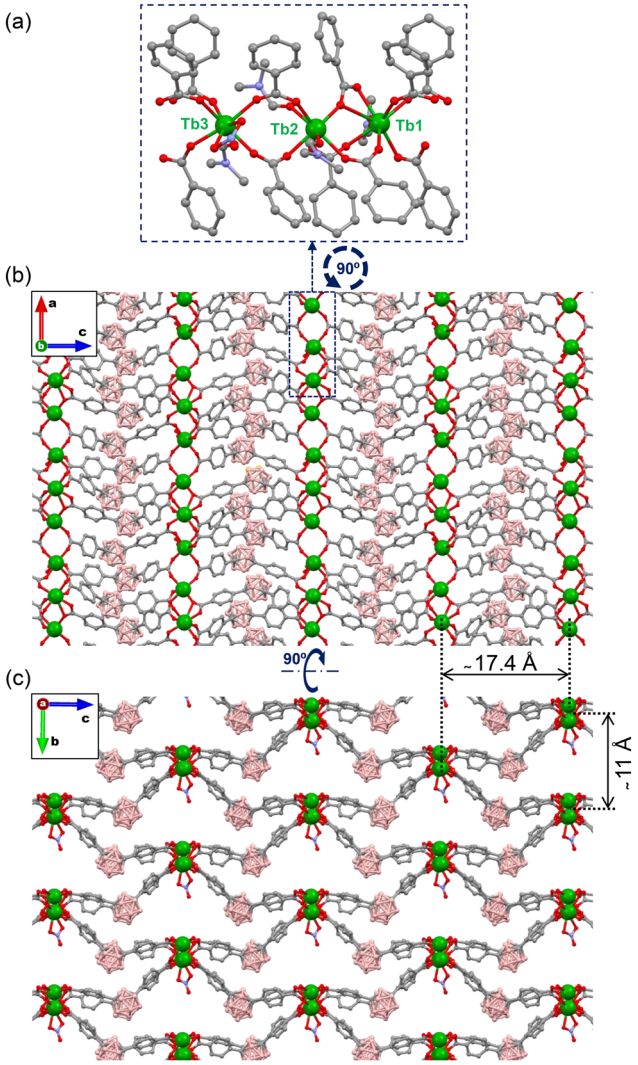

Fig. 1 Structure of {[(Tb)$_3$(*m*CB-L)$_4$(NO$_3$)(DMF)$_n$]·Solv} (***m*CB-Tb**). (a) View of the coordination of *m*CB-L to the three independent Tb atoms that are repeated along the structure. (b and c) Two perpendicular views of the extended 3D framework showing the 1D Tb chains. Distances between the polymeric 1D Tb chains are indicated. Colour code: Tb (green), O (red), B (pink), C (grey), and N (blue); H atoms (a–c) and DMF molecules (b–c) are omitted for clarity. The figure was prepared using Mercury.[97]

(Fig. S3 and S4†). The smaller surface area of ***m*CB-Dy** than that of ***m*CB-Tb** can be explained by the lanthanide contraction effect, which predicts a shrinkage of pore size as the atomic number of the lanthanide increases for an isostructural family of MOFs.[85]

Static magnetic results

To characterize the static magnetic behavior of the Dy and Tb carborane-based MOF, we measured the temperature dependence of the susceptibility times the temperature, $\chi T(T)$, at 0.1 T (Fig. 2a and c) and the field dependence of the magnetization $M(H)$ at different temperatures between T = 1.8 K and T = 21 K (Fig. 2b and d). For each compound, the $1/\chi(T)$ data in

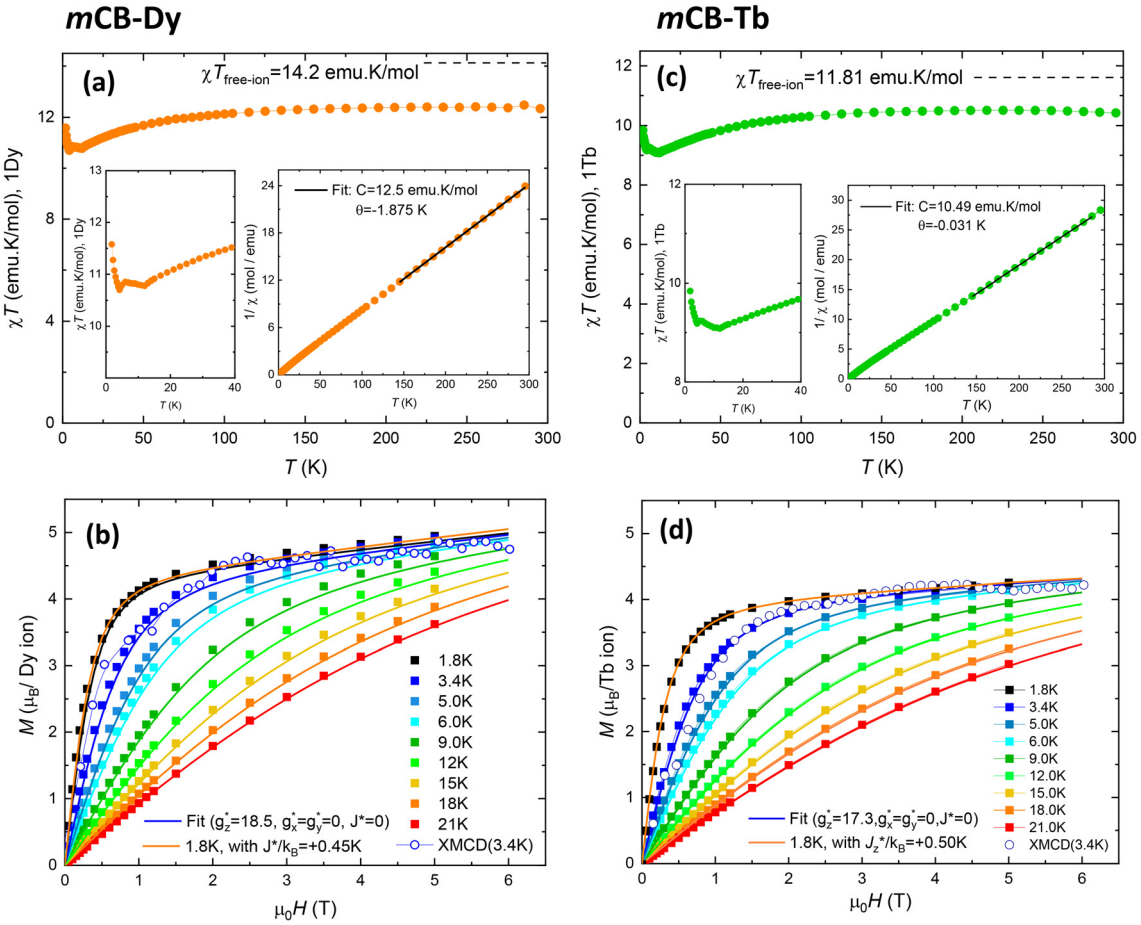

Fig. 2 Static magnetic properties for ***m*CB-Dy** (left) ***m*CB-Tb** (right). (a and c) Temperature dependence of the susceptibility times the temperature, $\chi T(T)$, at 0.1 T. Inset: Zoom of the low-T region. Additionally, inverse of the susceptibility, $1/\chi$ and fit to a Curie–Weiss law in the $T > 150$ K region; (b and d) bold symbols: field dependence of the magnetization per Ln ion, $M(H)$, measured at different temperatures between $T = 1.8$ K and 21 K; open circles: $m_{tot}(H)$/ion curve obtained at 3.4 K from XMCD(H). Lines: theoretical $M(H)$ curves calculated with Magpack within an Ising model of ions with an effective spin $S^* = 1/2$ and gyromagnetic values $g_x^* = g_y^* = 0$ and $g_z^* = 18.5$ for Dy ($g_z^* = 17.3$ for Tb), and negligible interactions ($J = 0$). The fit of the $M(H)$ at 1.8 K within a dimer model with a small, ferromagnetic constant $J^*/k_B = +0.45$ K (+0.50 K) for ***m*CB-Dy** (***m*CB-Tb**) is also shown.

the high-temperature region between 150 and 300 K were fit to a Curie–Weiss law, $1/\chi = C/(T - \theta)$, to obtain the Curie constant (C) and the Curie–Weiss temperature (θ); see Fig. 2a–c, insets.

For ***m*CB-Dy**, the $\chi T(T)$ product curve per Dy ion is shown in Fig. 2a. The room temperature value of 12.47 emu K mol^{-1} is somewhat below the $\chi T_{\text{free ion}} = g_J^2 J(J + 1)/8 = 14.2$ emu K mol^{-1} expected for Dy^{3+}($^6H_{15/2}$, $g_J = 4/3$). Upon decreasing the temperature, χT decreases smoothly until 10.7 emu K mol^{-1} at 4.2 K, and then increases, reaching 11.4 emu K mol^{-1} at 1.8 K. (It is noted that the small bulge appearing around 7 K is an instrumental artifact produced by the change of measurement regime mode.) This increase points to the existence of ferromagnetic interactions between the intra-chain Dy–Dy ions. On the other hand, the Curie–Weiss fit of the $1/\chi$ data (Fig. 2a, inset) yields a negative $\theta = -1.87$ K, evidencing the existence of overall antiferromagnetic (AF) interactions. Given that intra-chain short-range interactions are FM, this result suggests the existence of additional antiferromagnetic inter-chain Dy–Dy interactions, possibly of dipolar origin.

The isothermal magnetization curves measured for the ***m*CB-Dy** compound down to 1.8 K are shown in Fig. 2b. The $M(H)$ can be reasonably well fit under a model of non-interacting Dy ions with effective spin $S^* = 1/2$ and the anisotropic ground state with gyromagnetic factors $g_z^* = 18.5$ and $g_x^* = g_y^* = 0$, with a small van Vleck contribution ($M_{VV} = H \times 0.12\mu_B/T$).[86] Since XRD measurements evidence that there are three different Dy sites (Dy1, Dy2, Dy3), in this model g_z^* can be considered as an average of the anisotropic gyromagnetic factors of the three. At low T, the data fall slightly above the theoretical curves calculated for non-interacting ions ($J^* = 0$). A reasonable fit of $M(H)$ curve at 1.8 K is achieved assuming a simple model of dimer Dy–Dy ions interacting through a coupling constant of $J^*/k_B = +0.45$ K, thereby confirming the existence of weak, ferromagnetic (FM) intrachain as anticipated from $\chi T(T)$ results.

Qualitatively, the static magnetic properties of ***m*CB-Tb** are similar to those of the Dy counterpart. The $\chi T(T)$ curve per Tb (Fig. 2c) shows a room-temperature value of 10.47 emu K mol^{-1}, somewhat below the $\chi T_{\text{free ion}} = 11.8$ emu K mol^{-1}

expectation for Tb^{3+}(Tb^{3+}, $^7F_6$, g_J = 3/2). By lowering the temperature, the χT decreases until reaching 9.1 emu K mol^{-1} (10 K), and then increases to 9.8 emu K mol^{-1} at 1.8 K, again pointing to the presence of FM intra-chain Tb–Tb couplings. The Curie–Weiss fitting of $1/\chi$ data (Fig. 2c, inset) yields a negative, close to zero value of θ = −0.03 K (smaller than for ***m*CB-Dy**), suggesting near zero AF inter-chain interactions in the case of ***m*CB-Tb**. On the other hand, the isothermal $M(H)$ curves measured between 3.4 and 21 K (Fig. 2d) are well reproduced under a model of S^* = 1/2 spins with average, anisotropic gyromagnetic factors $g_z^* = 17.3$, $g_x^* = g_y^* = 0$, a van Vleck contribution of $M_{VV} = H \times 0.058\mu_B/T$ and negligible interactions (J^* = 0), while the 1.8 K is better fit including a small, ferromagnetic interaction of J^*/k_B = +0.50 K (see details in S2†).

XAS and XMCD characterization

X-ray absorption spectroscopy (XAS) and X-ray magnetic circular dichroism (XMCD) measurements were performed to further characterize the spectral characteristics across the $M_{4,5}$ edges of Dy in ***m*CB-Dy** and Tb in ***m*CB-Tb**, and obtain the orbital moment (m_L), spin moment (m_s) and total magnetic moment ($m_{tot} = m_L + m_s$) of each ion through application of the sum rules[87,88] adapted for lanthanides, following the procedure described by S. Tripathi.[89] The correction is needed to account for the large jj mixing between the $3d^{5/2}$ and $3d^{3/2}$ core levels, on the one hand, and the contribution of the $\langle T_z \rangle$ magnetic dipole term, on the other hand (see details in S3†).

Fig. 3 (left) shows the XAS and XMCD spectra measured across the $M_{4,5}$ edge of Dy in ***m*CB-Dy** at 3.4 K and 6 T, which show the typical spectral features for trivalent dysprosium. The XAS spectrum displays two pre-peaks (1290.81, 1292.79 eV), a main peak (1294.6) at M_5 and a shoulder (1297.3 eV), while M_4 includes two unresolved peaks (1328.1 and 1328.8 eV). The XMCD spectrum consists of negative peaks, across M_5 a main peak at 1294.6 eV, a minor peak at 1296.9 eV, and a small peak at M_4 (1327.8 eV). Application of the sum rules adapted for Dy(III) with a number of holes n_h = 5 yields $m_L = 2.53\mu_B$/ion, $m_s = 2.34\mu_B$/ion, and $m_{tot} = 4.87\mu_B$/ion at 3.4 K and 6 T.

The XAS and XMCD spectra across the $M_{4,5}$ edge of Tb in ***m*CB-Tb** at 3.4 K and 6 T (Fig. 3, right) show the expected features for terbium(III). The XAS spectrum exhibits a pre-peak (1235.19 eV) and two main peaks (1241, 1242.1 eV) and shoulder in the M_5 region, while M_4 consists of a peak at 1270.53 eV and shoulder (1273.2 eV). The XMCD spectrum contains a primary negative peak at 1242.31 eV in the M_5 region and a minor peak at 1245.3 eV, and three features in the M_4 region (1273.4–1276.7 eV). The sum rules applied to Tb(III), with n_h = 6, yield in this case $m_L = 1.47\mu_B$/ion, $m_s = 2.89\mu_B$/ion and $m_{tot} = 4.36\mu_B$/ion, at 3.4 K and 6 T. Thus, the determined orbital magnetic moment for Dy is larger than for Tb in these *m*CB-Ln MOFs.

In addition, the field dependence of the total magnetic moment, $m_{tot}(H)$/ion, of Dy in ***m*CB-Dy** and Tb in ***m*CB-Tb** at 3.4 K was determined by following the intensity of the XMCD

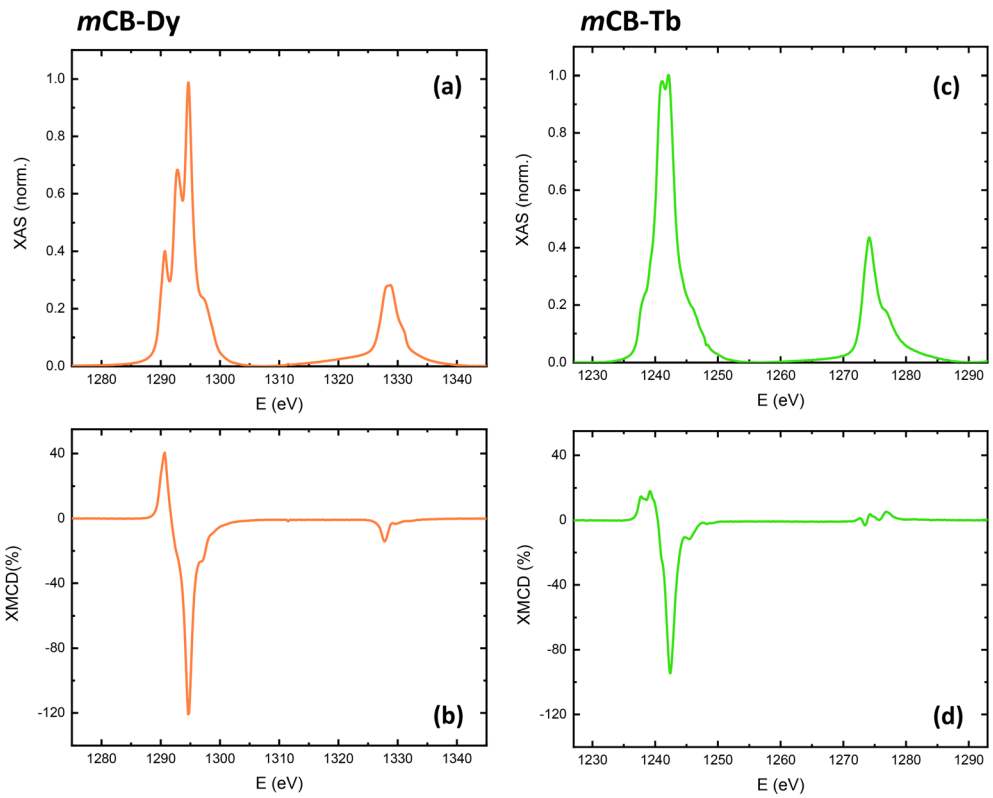

Fig. 3 XAS and XMCD characterization of ***m*CB-Dy** (left) and ***m*CB-Tb** (right). Normalized, background-subtracted XAS (top) and XMCD (bottom) spectra measured across the $M_{4,5}$ edge of Dy (a and b) and Dy (c and d) at 6 T at T = 3.4 K.

(H) peak at the M_5 edge between −6 T and 6 T, and scaling the curve with the m_{tot}(6 T) value obtained from the sum rules. As shown in Fig. 2b and d (open circles), the $m_{tot}(H)$/ion curves determined by XMCD are in good agreement with the $M(H)$ curves measured by SQUID at 3.4 K, within the experimental noise of the technique.

Heat capacity

The temperature dependence of the specific heat, $c_p(T)$, measured down to 0.3 K at different applied magnetic fields ranging between 0 and 3 T for the two studied compounds is shown in Fig. 4 (top). In both cases, the magnetic heat capacity contribution peaks, $c_m(T, H)$, are observed over the lattice contribution $c_L(T)$.

For ***m*CB-Dy**, the $c_m(T)$ curve at $H = 0$ shows a Schottky-type broad anomaly with a center lower than 0.3 K. Upon increasing the applied field, the $c_m(T)$ peak shifts to higher temperatures, and an increase of the c_m signal at the lowest temperature is hinted (Fig. 5a).

On the other hand, the $c_m(T, 0)$ curve of ***m*CB-Tb** also shows a Schottky-type anomaly, which is centered at a higher temperature (T_{sc} = 0.5 K). With increasing field, this peak also shifts

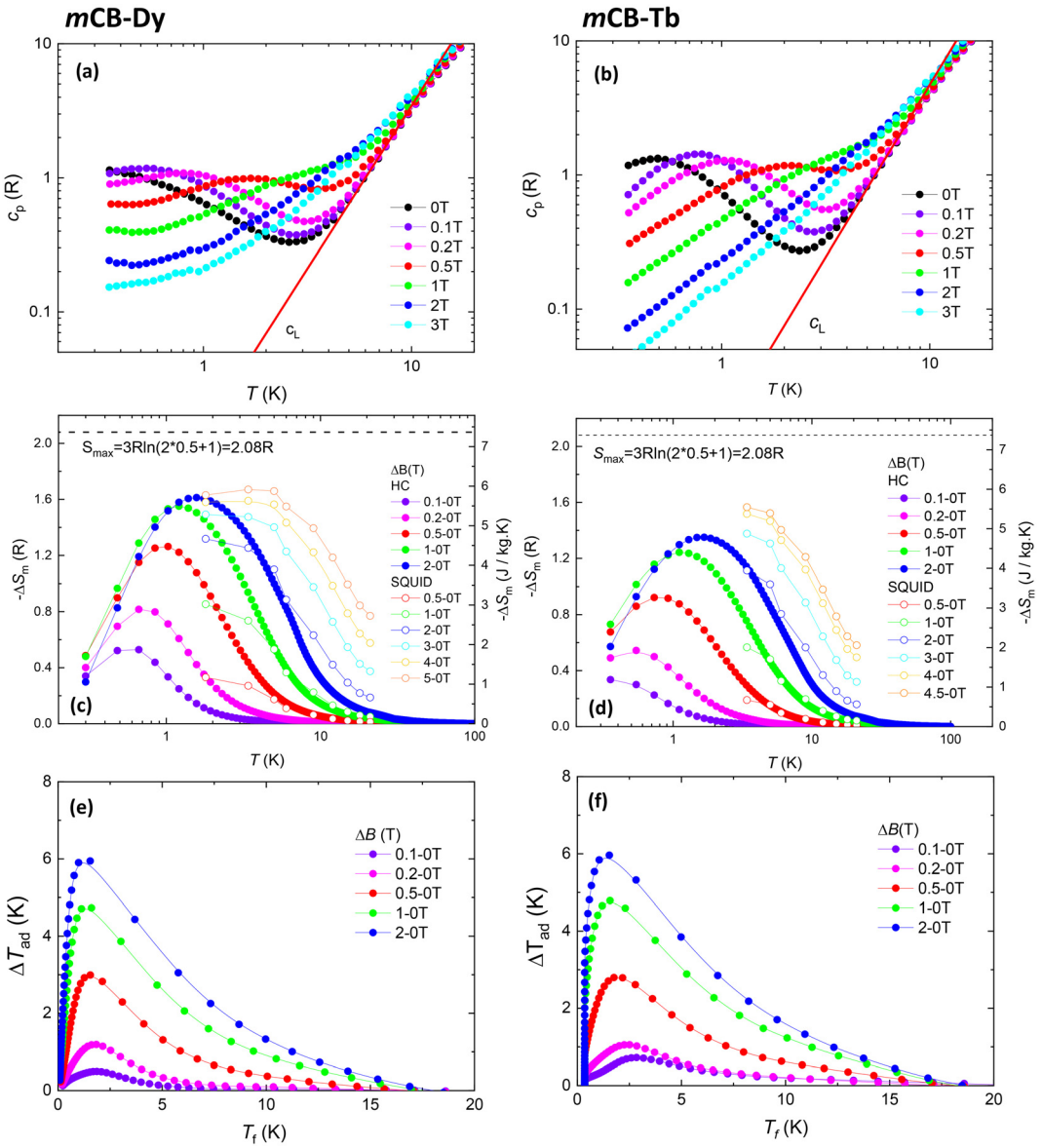

Fig. 4 Heat capacity and MCE characterization for ***m*CB-Dy** (left) ***m*CB-Tb** (right). (a, b) Specific heat as a function of the temperature, $c_p(T)$, at different applied magnetic fields. The line corresponds to the lattice contribution, $c_L(T) = AT^n$, (A/R = 0.01265 $K^{-2.57}$, n = 2.57 for ***m*CB-Dy**; A/R = 0.0128 $K^{-2.43}$, n = 2.43 for ***m*CB-Tb**); (c, d) temperature dependence of the magnetic entropy change, $-\Delta S_m$, obtained from the $c_m(T) = c_p(T) - c_L(T)$ data for the indicated magnetic field changes ΔB. The dashed line represents the maximum full entropy content of the Dy and Tb MOFs, $S_{max} = 3R \ln(2S + 1)$, containing three Ln^{3+} ions with $S^* = 1/2$ at low T; (e, f) temperature dependence of the adiabatic temperature change $\Delta T_{ad}(T)$ for the indicated field changes ΔB.

to a higher T, but unlike in the former compound, no further contribution at low temperatures is observed (Fig. 5b). No magnetic ordering is observed in either of the two MOFs down to the lowest measured temperature of 0.4 K.

The heat capacity data allowed us to characterize the magnetocaloric effect (MCE). The magnetic entropy change $-\Delta S_m(T, \Delta B)$ for selected magnetic field changes $\Delta B = \mu_0(H_f - H_i)$ is shown in Fig. 4c and d for ***m*CB-Dy** and ***m*CB-Tb**, respectively. The maximum final field $\mu_0 H_f$ = 2 T is chosen to compare with other values in the literature.[50,51,90] This field is taken as the standard, since it is reachable with permanent magnets in the potential application as a magnetic refrigerator. For ΔB = 2-0 T, we find a maximum value of $-\Delta S_m^{max}$ = 5.71 J kg^{-1} K^{-1} at T^{max} = 1.61 K for ***m*CB-Dy** and $-\Delta S_m^{max}$ = 4.78 J kg^{-1} K^{-1} at T^{max} = 1.67 K for ***m*CB-Tb**. Considering the full width at half maximum of the $-\Delta S_m$ curve, δT_{FWHM}, the obtained relative cooling power is RCP = $-\Delta S_m^{max} \times \delta T_{FWHM}$ = 32.6 J kg^{-1} K^{-1} (***m*CB-Dy**) and 27.9 J kg^{-1} K^{-1} (***m*CB-Tb**). Besides, the adiabatic temperature change $\Delta T_{ad}(T) = T_f - T_i$ has been calculated and is shown in Fig. 4e and f. For ΔB = 2–0 T the temperature change reaches a maximum ΔT_{ad}^{max} = 5.94 K at T = 1.22 K (***m*CB-Dy**) and ΔT_{ad}^{max} = 5.87 K at T = 1.36 K (***m*CB-Tb**).

Alternatively, the magnetic entropy change was extracted from the $M(H)$ isotherms recorded at different temperatures, using Maxwell's equations.[91] This method allowed us to characterize the MCE for a higher ΔB of 5–0 T. The maximum magnetic entropy change obtained was $-\Delta S_m$(5 T) = 5.92 J K^{-1} kg^{-1} (***m*CB-Dy**) and 5.55 J K^{-1} kg^{-1} (***m*CB-Tb**). The magnetic entropy change values for these compounds are smaller than that previously obtained for the gadolinium (S = 7/2) analogue of the same family, ***m*CB-Gd**, which exhibited a value of $-\Delta S_m^{max}$ = 16.23 J kg^{-1} K^{-1} at T = 0.8 K for ΔB = 2 T.[92] However, interestingly, the MCE peak for the Dy and Tb MOFs occurs at a higher temperature than for Gd, consistent with previous findings in the literature,[51–53] thus extending the operating

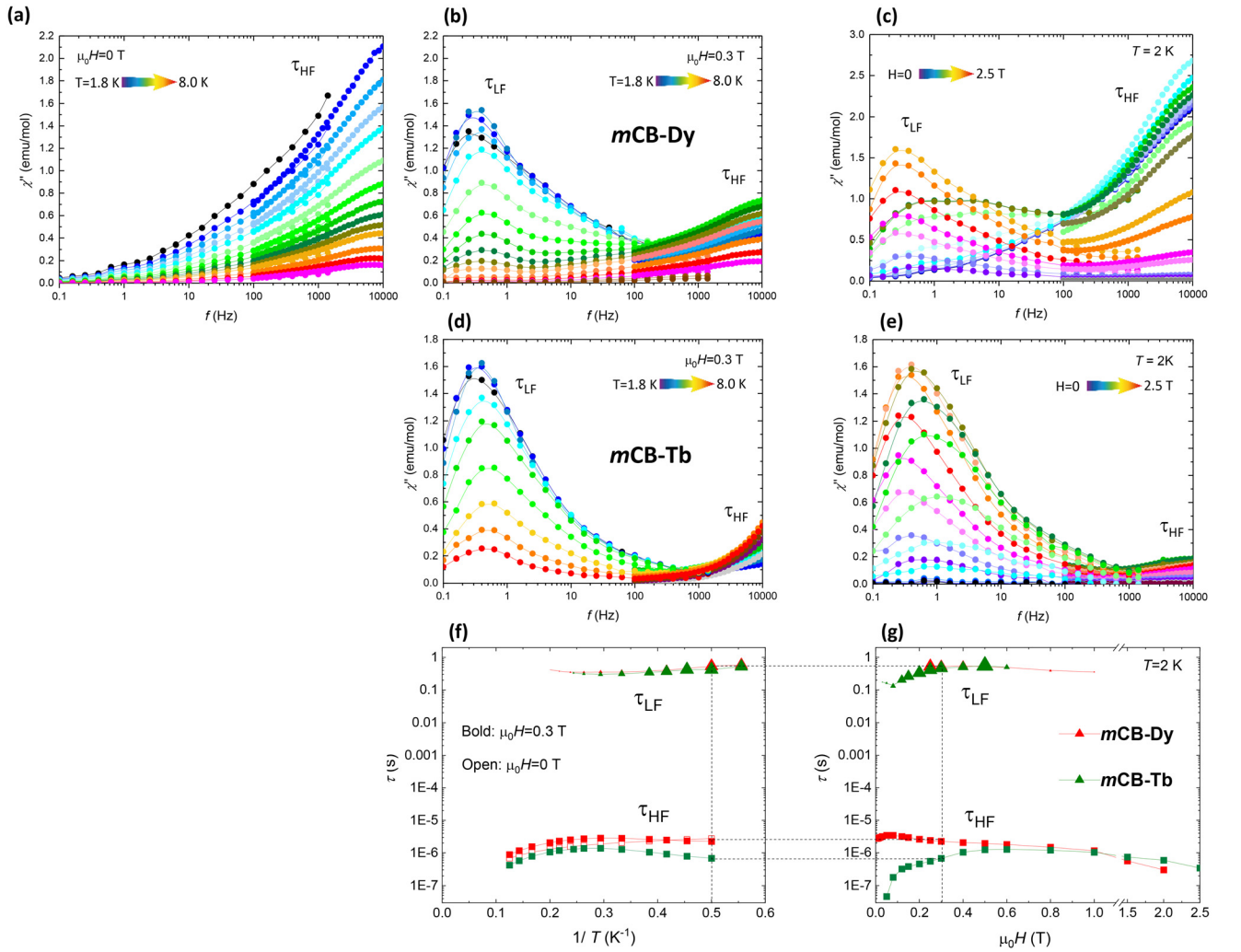

Fig. 5 Ac susceptibility results for the ***m*CB-Dy** and ***m*CB-Tb** MOFs: (a) $\chi''(f, T)$ at H = 0; (b and d) $\chi''(f, T)$ at $\mu_0 H$ = 3 T; (c), (e) $\chi''(f, H)$ at constant T = 2 K; (f) relaxation time *vs.* inverse of the temperature, and (g) relaxation time as a function of the applied field, at T = 2.0 K. The relaxation times for the two observed processes are denoted as τ_{LF} and τ_{HF}.

temperature for magnetic cooling. Moreover, we emphasize that understanding the magnetocaloric performance of these homonuclear *m*CB-Ln (Ln = Dy, Tb) compounds is crucial, in view of the subsequent design of multifunctional mixed {GdLn} MOFs.[92]

Dynamic results

Alternating current (ac) magnetic susceptibility measurements as a function of frequency (f = 0.1–10^4 Hz) at different temperatures between 1.8 and 8 K and applied magnetic fields from 0 to 2.5 T were performed to characterize spin dynamic relaxation of the studied carborane-based MOFs.

For ***m*CB-Dy**, a frequency-dependent out-of-phase susceptibility $\chi''(f, T)$ between 1.8 and 18 K was observed even at zero applied field (Fig. 5a). The $\chi''(f, H)$ measurements performed at constant T = 2 K show the evolution of the processes under magnetic fields ranging from 0 to 2.5 T (Fig. 5c). Under the application of a constant optimum field of 0.3 T (Fig. 5b), the χ'' curves show a clear peak at low frequencies (LF) at *ca.* 0.3 Hz, a shoulder at 0.5 Hz, and the tail of a high frequency (HF) peak. In the case of the ***m*CB-Tb** compound, no out-of-phase signal was detected at H = 0. Under the application of a magnetic field, the $\chi''(f, T, H)$ curves deployed a large peak at a low frequency, and the emergence of a second relaxation process for f > 10 kHz (Fig. 5d and e).

The relaxation time of the low-frequency processes as a function of the inverse of the temperature and the magnetic field $\tau_{LF}(1/T, H)$ were determined from the maximum of the $\chi''(f)$ peaks, at which $\omega\tau = 1$ ($\omega = 2\pi f$). For the high-frequency process, for which only the tails of the χ'' peak were visible within the measurement frequency window, the relaxation time was estimated as $\tau_{HF} = (1/2\pi f)(\chi''/\chi')$, at a constant f fulfilling the condition $\omega\tau \ll 1$. The relaxation times of the different processes as a function of the inverse of the temperature and the field, $\tau_{LF}(1/T, H)$ and $\tau_{HF}(1/T, H)$, determined for the two compounds are depicted in Fig. 5f and g.

The HF process observed in the ***m*CB-Dy** compound with a $\tau_{HF} \approx 5 \times 10^{-5}$ s at low temperatures is associated with a fast mechanism of relaxation through quantum tunneling of the magnetization (QTM). At increasing temperatures, the $\tau_{HF}(1/T)$ exhibits a decreasing trend, indicating that this mechanism is being replaced by a thermally activated mechanism, $\tau = \tau_0 \exp(U_{eff}/k_BT)$; however, the data available do not afford obtaining the activation energy (U_{eff}) reliably, neither at H = 0 nor at H = 0.3 T.

The fact that slow relaxation of magnetization under zero applied field only appears in ***m*CB-Dy** and not in ***m*CB-Tb** may be attributed to the heightened anisotropy of Ln ions in the former, as suggested by the larger g_z^* value obtained from $M(H)$ fits, and supported by the larger orbital magnetic moment m_L, as determined by XMCD.

On the other hand, the temperature and field dependencies of the low-frequency processes observed in the two compounds are characteristic of a direct, bottlenecked slow relaxation mechanism. This type of relaxation process has been frequently documented in previous studies of coordination polymers.[93–96]

4. Conclusions

The magnetic and MCE properties of two isostructural MOFs, {[(Ln)$_3$(*m*CB-L)$_4$(NO$_3$)(DMF)$_n$]·Solv} (Ln = Dy, Tb) were characterized by combining dc magnetometry, ac magnetometry, XAS–XMCD and heat capacity measurements. The porous 3D structure of these MOFs is constructed by polymeric 1D chains of Ln ions in three different coordination environments (Ln1, Ln2, Ln3) within the SBU, interconnected to adjacent chains through bulky carborane linkers. Static magnetic results revealed that these MOFs can be modeled at low temperature as a system of S^* = 1/2 Ising spins weakly coupled ferromagnetically along the chain and simultaneously coupled to Ln ions in neighbouring chains through weak antiferromagnetic dipolar interactions. XAS and XMCD measurements were used to spectroscopically characterize the Ln(III) ions in the two MOFs and determine the average spin, orbital and total magnetic moments. The obtained m_L values, together with the gyromagnetic values obtained from the theoretical fitting of the low-temperature $M(H)$ curves, evidence the larger anisotropic character of the Dy ion compared to Tb in these *m*CB-based MOFs. As expected in this scenario, thermally activated SMM behavior under zero dc field is only observed for the Dy complex, while relaxation through very slow, direct processes under application of a 0.3 T field is observed in both MOFs. Direct MCE characterization through heat capacity measurements revealed a maximum $-\Delta S_m^{max}$ of 5.71 J kg^{-1} K^{-1} at 1.61 K for ***m*CB-Dy** and 4.78 J kg^{-1} K^{-1} at 1.67 K for ***m*CB-Tb**, for a field change of 2–0 T. While these magnetic entropy changes are modest compared to the value achieved by the Gd analogue, the MCE peak occurs at a higher temperature, underscoring the potential of using anisotropic ions, alone or mixed with Gd, to design magnetocaloric materials for different cryogenic temperature regions. The two reported carborane-based MOFs emerge as interesting multifunctional materials, combining MCE and magnetic relaxation and high quantum yield luminescent emission in the visible light region for the Tb analogue.

Conflicts of interest

There are no conflicts of interest to declare.

Acknowledgements

This work was financially supported by the Spanish Ministerio de Ciencia e Innovación projects PID2022-138492NB-I00 and PID2022-136892NB-I00, the Generalitat de Catalunya (2021/SGR/00442), and the Gobierno de Aragón (project RASMIA E12-23R). Zhen Li acknowledges the China Scholarship Council (CSC) for his PhD grant (201808310071). The authors would like to acknowledge the use of Servicio General de Apoyo a la Investigación-SAI, Universidad de Zaragoza. XAS and XMCD experiments were performed at the BOREAS beam-

line of the ALBA synchrotron with the support of ALBA staff (experiment number 2022085925).

References

1 H. Li, M. Eddaoudi, M. O'Keeffe and O. M. Yaghi, *Nature*, 1999, **402**, 276–279.
2 O. M. Yaghi, M. O'Keeffe, N. W. Ockwig, H. K. Chae, M. Eddaoudi and J. Kim, *Nature*, 2003, **423**, 705–714.
3 O. K. Farha, A. O. Yazaydın, I. Eryazici, C. D. Malliakas, B. D. Hauser, M. G. Kanatzidis, S. T. Nguyen, R. Q. Snurr and J. T. Hupp, *Nat. Chem.*, 2010, **2**, 944–948.
4 X. J. Wang, X. Zhang, R. Pandharkar, J. F. Lyu, D. Ray, Y. Yang, S. Kato, J. Liu, M. C. Wasson, T. Islamoglu, Z. Li, J. T. Hupp, L. Gagliardi and O. K. Farha, *ACS Catal.*, 2020, **10**, 8995–9005.
5 D. Q. Yuan, D. Zhao, D. F. Sun and H. C. Zhou, *Angew. Chem., Int. Ed.*, 2010, **49**, 5357–5361.
6 X. Zhang, V. Vieru, X. Feng, J.-L. Liu, Z. Zhang, B. Na, W. Shi, B.-W. Wang, A. K. Powell, L. F. Chibotaru, S. Gao, P. Cheng and J. R. Long, *Angew. Chem., Int. Ed.*, 2015, **54**, 9861–9865.
7 K. Liu, X. Zhang, X. Meng, W. Shi, P. Cheng and A. K. Powell, *Chem. Soc. Rev.*, 2016, **45**, 2423–2439.
8 G. Mínguez Espallargas and E. Coronado, *Chem. Soc. Rev.*, 2018, **47**, 533–557.
9 Y. Zhang, S. Yuan, G. Day, X. Wang, X. Yang and H.-C. Zhou, *Coord. Chem. Rev.*, 2018, **354**, 28–45.
10 Y. Cui, B. Chen and G. Qian, *Coord. Chem. Rev.*, 2014, **273–274**, 76–86.
11 Z. Qu, D. Wu, J. Jin, G. Yang and Y.-Y. Wang, *J. Solid State Chem.*, 2022, **309**, 123003.
12 Z. Li, R. Núñez, M. E. Light, E. Ruiz, F. Teixidor, C. Viñas, D. Ruiz-Molina, C. Roscini and J. G. Planas, *Chem. Mater.*, 2022, **34**, 4795–4808.
13 Y. Guo, Z. Han, H. Min, Z. Chen, T. Sun, L. Wang, W. Shi and P. Cheng, *Inorg. Chem.*, 2021, **60**, 9192–9198.
14 J.-M. Li, R. Huo, X. Li and H.-L. Sun, *Inorg. Chem.*, 2019, **58**, 9855–9865.
15 Q. Lin, W. Xie, Z. Zong, Z. Liu, Y. Sun and L. Liang, *New J. Chem.*, 2021, **45**, 7382–7389.
16 S. Mohapatra, B. Rajeswaran, A. Chakraborty, A. Sundaresan and T. K. Maji, *Chem. Mater.*, 2013, **25**, 1673–1679.
17 D. B. Kanzariya, M. Y. Chaudharya and T. K. Pal, *Dalton Trans.*, 2023, **52**, 7383–7404.
18 G. Lorusso, J. W. Sharples, E. Palacios, O. Roubeau, E. K. Brechin, R. Sessoli, A. Rossin, F. Tuna, E. J. L. McInnes, D. Collison and M. Evangelisti, *Adv. Mater.*, 2013, **25**, 4653–4656.
19 G. Lorusso, E. Natividad, M. Evangelisti and O. Roubeau, *Mater. Horiz.*, 2019, **6**, 144–156.
20 M. Falsaperna and P. Saines, *Dalton Trans.*, 2022, **51**, 3394–3410.
21 P. Konieczny, W. Sas, D. Czernia, A. Pacanowska, M. Fitta and R. Pełka, *Dalton Trans.*, 2022, **51**, 12762–12780.
22 S. Kumar, G. Gabarró-Riera, A. Arauzo, J. Hrubý, S. Hill, L. Bogani, J. Rubio-Zuazo, J. Jover, E. Bartolomé and E. C. Sañudo, *J. Mater. Chem. A*, 2024, **12**, 6269–6279.
23 C.-L. Chen, C. Wang, X.-Y. Zheng, R. Zhang, Y. Xu, G.-L. Zhuang, L.-S. Long, L.-S. Zheng, X.-J. Kong and Y. Cao, *J. Am. Chem. Soc.*, 2023, **145**, 16983–16987.
24 E. Coronado, *Nat. Rev. Mater.*, 2020, **5**, 87–104.
25 M. J. Graham, J. M. Zadrozny, M. S. Fataftah and D. E. Freedman, *Chem. Mater.*, 2017, **29**, 1885–1897.
26 E. Bartolomé, A. Arauzo, S. Fuertes, L. Navarro-Spreafica, P. Sevilla, H. F. Cortés, N. Settineri, S. J. Teat and E. C. Sañudo, *Dalton Trans.*, 2023, **52**, 7258–7270.
27 E. Bartolomé, A. Arauzo, S. Herce, A. Palau, N. Mestres, S. Fuertes, P. Sevilla, N. S. Settineri, L. Navarro-Spreafico, J. González and E. C. Sañudo, *Molecules*, 2021, **26**, 5503.
28 A. Arauzo, L. Gasque, S. Fuertes, C. Tenorio, S. Bernès and E. Bartolomé, *Dalton Trans.*, 2020, **49**, 13671–13684.
29 N. Ishikawa, M. Sugita, T. Ishikawa, S. Y. Koshihara and Y. Kaizu, *J. Am. Chem. Soc.*, 2003, **125**, 8694–8695.
30 E. Bartolomé, A. Arauzo, J. Luzón, J. Bartolomé and F. Bartolomé, in *Handbook of Magnetic Materials*, ed. E. Brück, Elsevier, 2017, pp. 1–289.
31 L. Sorace and D. Gatteschi, in *Lanthanides and Actinides in Molecular Magnetism*, ed. R. Layfield and M. Murugesu, Wiley-VCH, 2015.
32 Z. Zhu, C. Zhao, T. Feng, X. Liu, X. Ying, X.-L. Li, Y.-Q. Zhang and J. Tang, *J. Am. Chem. Soc.*, 2021, **143**, 10077–10082.
33 F. S. Guo, B. M. Day, Y. C. Chen, M. L. Tong, A. Mansikkamäki and R. A. Layfield, *Science*, 2018, **362**, 1400–1403.
34 A. Gaita-Ariño, F. Luis, S. Hill and E. Coronado, *Nat. Chem.*, 2019, **11**, 301–309.
35 M. D. Jenkins, Y. Duan, B. Diosdado, J. J. García-Ripoll, A. Gaita-Ariño, C. Giménez-Saiz, P. J. Alonso, E. Coronado and F. Luis, *Phys. Rev. B*, 2017, **95**, 064423.
36 F. Luis, P. J. Alonso, O. Roubeau, V. Velasco, D. Zueco, D. Aguilà, J. I. Martínez, L. A. Barrios and G. Aromí, *Commun. Chem.*, 2020, **3**, 176.
37 M. Urdampilleta, S. Klyatskaya, M. Ruben and W. Wernsdorfer, *Phys. Rev. B: Condens. Matter Mater. Phys.*, 2013, **87**, 195412.
38 C. Godfrin, A. Ferhat, R. Ballou, S. Klyatskaya, M. Ruben, W. Wernsdorfer and F. Balestro, *Phys. Rev. Lett.*, 2017, **119**, 187702.
39 J. J. Baldovi, E. Coronado and A. Gaita-Arino, *Chem. – Eur. J.*, 2014, **20**, 10695–10702.
40 J. López-Cabrelles, L. Escalera-Moreno, Z. Hu, H. Prima-García, G. Mínguez-Espallargas, A. Gaita-Ariño and E. Coronado, *Inorg. Chem.*, 2021, **60**, 8575–8580.
41 A. Urtizberea, E. Natividad, P. J. Alonso, M. A. Andrés, I. Gascón, M. Goldmann and O. Roubeau, *Adv. Funct. Mater.*, 2018, **28**, 1801695.
42 F. Ma, R. Sun, A.-H. Sun, J. Xiong, H.-L. Sun and S. Gao, *Inorg. Chem. Front.*, 2020, **7**, 930–938.

43 C. Zhang, X. Ma, P. Cen, X. Jin, J. Yang, A. Y.-Q. Zhang, J. Ferrando-Soria, E. Pardo and X. Liu, *Dalton Trans.*, 2020, **49**, 14123–14132.
44 L. Li, Y. Fang, S. Liu, M. Hu and W. Wang, *J. Rare Earths*, 2023, **41**, 100–107.
45 C. Bai, C.-T. Li, H.-M. Hu, B. Liu, J.-D. Li and G. Xue, *Dalton Trans.*, 2019, **48**, 814–817.
46 Z. Chen, B. Zhao, P. Cheng, X. Q. Zhao, W. Shi and Y. Song, *Inorg. Chem.*, 2009, **48**, 3493–3495.
47 T. Yang, S. Wang, C. Lin, X. Wang, B. Zhu and D. Wu, *Dalton Trans.*, 2021, **50**, 1293–1299.
48 A. Calahorro, I. Oyarzabal, B. Fernandez, J. Seco, T. Tian and D. Fairen-Jimenez, *Dalton Trans.*, 2016, **45**, 591–598.
49 R. Gao, F. Guo, N. Bai, Y. Wu, F. Yang and J. Liang, *Inorg. Chem.*, 2016, **55**, 11323–11330.
50 R. J. C. Dixey and P. J. Saines, *Inorg. Chem.*, 2018, **57**, 12543–12551.
51 P. J. Saines, J. A. M. Paddison, P. M. M. Thygesen and M. G. Tucker, *Mater. Horiz.*, 2015, **2**, 528–535.
52 P. W. Doheny, S. J. Cassidy and P. J. Saines, *Inorg. Chem.*, 2022, **61**, 4957–4964.
53 S. Kim, R. Muhammad, K. Son and H. Oh, *Inorg. Chem.*, 2023, **62**, 2994–2999.
54 Y.-L. Hou, G. Xiong, P.-F. Shi, R.-R. Cheng, J.-Z. Cui and B. Zhao, *Chem. Commun.*, 2013, **49**, 6066–6068.
55 H.-C. Hu, X.-M. Kang, C.-S. Cao, P. Cheng and B. Zhao, *Chem. Commun.*, 2015, **51**, 10850–10853.
56 J. González, P. Sevilla, G. Gabarró-Riera, J. Jover, J. Echeverría, S. Fuertes, A. Arauzo, E. Bartolomé and E. C. Sañudo, *Angew. Chem., Int. Ed.*, 2021, **60**, 12001–12006.
57 F.-G. Chen, W. Xu, J. Chen, H.-P. Xiao, H.-Y. Wang, Z. Chen and J.-Y. Ge, *Inorg. Chem.*, 2022, **61**, 5388–5396.
58 X.-Q. Ji, R. Sun, J. Xiong, H.-L. Sun and S. Gao, *J. Mater. Chem. C*, 2021, **9**, 15858–15867.
59 I. Oyarzabal, B. Fernández, J. Cepeda, S. Gómez-Ruiz, A. J. Calahorro, J. M. Seco and A. Rodríguez-Diéguez, *CrystEngComm*, 2016, **18**, 3055–3063.
60 R. Li, R. Li, X. Liu, X. Chang and X. Feng, *RSC Adv.*, 2020, **10**, 6192–6199.
61 Q.-Y. Liu, Y.-L. Li, Y.-L. Wang, C.-M. Liu, L.-W. Ding and Y. Liu, *CrystEngComm*, 2014, **16**, 486–491.
62 S. Wang, T. Cao, H. Yan, Y. Li, J. Lu, R. Ma, D. Li, J. Dou and J. Bai, *Inorg. Chem.*, 2016, **55**, 5139–5151.
63 L. Gan, E. Andres-Garcia, G. Mínguez Espallargas and J. G. Planas, *ACS Appl. Mater. Interfaces*, 2023, **15**, 5309–5316.
64 M. Y. Tsang, S. Rodríguez-Hermida, K. C. Stylianou, F. Tan, D. Negi, F. Teixidor, C. Viñas, D. Choquesillo-Lazarte, C. Verdugo-Escamilla, M. Guerrero, J. Sort, J. Juanhuix, D. Maspoch and J. Giner Planas, *Cryst. Growth Des.*, 2017, **17**, 846–857.
65 S. Rodríguez-Hermida, M. Y. Tsang, C. Vignatti, K. C. Stylianou, V. Guillerm, J. Pérez-Carvajal, F. Teixidor, C. Viñas, D. Choquesillo-Lazarte, C. Verdugo-Escamilla, I. Peral, J. Juanhuix, A. Verdaguer, I. Imaz, D. Maspoch and J. Giner Planas, *Angew. Chem., Int. Ed.*, 2016, **55**, 16049–16053.
66 Z. Li, X.-B. Li, M. E. Light, A. E. Carrillo, A. Arauzo, M. Valvidares, C. Roscini, F. Teixidor, C. Viñas, F. Gándara, E. Bartolomé and J. G. Planas, *Adv. Funct. Mater.*, 2023, **33**, 2307369.
67 L. Gan, M. T. Nord, J. M. Lessard, N. Q. Tufts, A. Chidambaram, M. E. Light, H. Huang, E. Solano, J. Fraile, F. Suárez-García, C. Viñas, F. Teixidor, K. C. Stylianou and J. G. Planas, *J. Am. Chem. Soc.*, 2023, **145**, 13730–13741.
68 Z. Li, D. Choquesillo-Lazarte, J. Fraile, C. Viñas, F. Teixidor and J. G. Planas, *Dalton Trans.*, 2022, **51**, 1137–1143.
69 J. Soldevila-Sanmartín, E. Ruiz, D. Choquesillo-Lazarte, M. E. Light, C. Viñas, F. Teixidor, R. Núñez, J. Pons and J. G. Planas, *J. Mater. Chem. C*, 2021, **9**, 7643–7657.
70 Z. Li, J. Fraile, C. Viñas, F. Teixidor and J. G. Planas, *Chem. Commun.*, 2021, **57**, 2523–2526.
71 L. Gan, A. Chidambaram, P. G. Fonquernie, M. E. Light, D. Choquesillo-Lazarte, H. Huang, E. Solano, J. Fraile, C. Viñas, F. Teixidor, J. A. R. Navarro, K. C. Stylianou and J. G. Planas, *J. Am. Chem. Soc.*, 2020, **142**, 8299–8311.
72 L. Gan, P. G. Fonquernie, M. E. Light, G. Norjmaa, G. Ujaque, D. Choquesillo-Lazarte, J. Fraile, F. Teixidor, C. Viñas and J. G. Planas, *Molecules*, 2019, **24**, 3204.
73 F. Tan, A. López-Periago, M. E. Light, J. Cirera, E. Ruiz, A. Borrás, F. Teixidor, C. Viñas, C. Domingo and J. G. Planas, *Adv. Mater.*, 2018, **30**, 1800726.
74 J. Poater, C. Viñas, I. Bennour, S. Escayola, M. Solà and F. Teixidor, *J. Am. Chem. Soc.*, 2020, **142**, 9396–9407.
75 J. Poater, M. Solà, C. Viñas and F. Teixidor, *Angew. Chem., Int. Ed.*, 2014, **53**, 12191–12195.
76 J. Poater, C. Viñas, M. Solà and F. Teixidor, *Nat. Commun.*, 2022, **13**, 3844.
77 J. Plesek, *Chem. Rev.*, 1992, **92**, 269–278.
78 M. Scholz and E. Hey-Hawkins, *Chem. Rev.*, 2011, **111**, 7035–7062.
79 R. N. Grimes, *Carboranes*, Academic Press, 2016.
80 F. Teixidor and D. E. Kaufmann, *Science of Synthesis: Houben-Weyl Methods of Molecular Transformations*, Georg Thieme Verlag, Stuttgart, 5th edn, 2015, vol. 6.
81 S. Fujii, *MedChemComm*, 2016, **7**, 1082–1092.
82 F. Issa, M. Kassiou and L. M. Rendina, *Chem. Rev.*, 2011, **111**, 5701–5722.
83 J. F. Valliant, K. J. Guenther, A. S. King, P. Morel, P. Schaffer, O. O. Sogbein and K. A. Stephenson, *Coord. Chem. Rev.*, 2002, **232**, 173–230.
84 M. A. Fox, *Icosahedral carborane derivatives*, Doctoral thesis, Durham University, 1991.
85 L. Han, T. Pham, M. Zhuo, K. A. Forrest, S. Suepaul, B. Space, M. J. Zaworotko, W. Shi, Y. Chen, P. Cheng and Z. Zhang, *ACS Appl. Mater. Interfaces*, 2019, **11**, 23192–23197.
86 J. H. van Vleck, *Phys. Rev.*, 1928, **31**, 587.
87 P. Carra, B. T. Thole, M. Altarelli and X. Wang, *Phys. Rev. Lett.*, 1993, **70**, 694–697.

88 B. Thole, P. Carra, F. Sette and G. van der Laan, *Phys. Rev. Lett.*, 1992, **68**, 1943–1946.
89 S. Tripathi, *Max-Planck-Institut für Intelligente Systeme*, PhD Thesis, Stuttgart, 2018.
90 A. Arauzo, A. Lazarescu, S. Shova, E. Bartolomé, R. Cases, J. Luzón, J. Bartolomé and C. Turta, *Dalton Trans.*, 2014, **43**, 12342–12356.
91 M. Evangelisti and E. K. Brechin, *Dalton Trans.*, 2010, **39**, 4672–4676.
92 Manuscript in preparation, 2024.
93 E. Bartolomé, J. Bartolomé, S. Melnic, D. Prodius, S. Shova, A. Arauzo, J. Luzón, F. Luis and C. Turta, *Dalton Trans.*, 2013, **42**, 10153–10171.
94 E. Bartolomé, A. Arauzo, J. Luzón, S. Melnic, S. Shova, D. Prodius, J. Bartolomé, A. Amann, M. Nallaiyan and S. Spagna, *Dalton Trans.*, 2019, **48**, 5022–5034.
95 E. Bartolomé, J. Bartolomé, S. Melnic, D. Prodius, S. Shova, A. Arauzo, J. Luzón, L. Badía-Romano, F. Luis and C. Turta, *Dalton Trans.*, 2014, **43**, 10999–11013.
96 E. Bartolomé, J. Bartolomé, A. Arauzo, J. Luzón, L. Badía, R. Cases, F. Luis, S. Melnic, D. Prodius, S. Shova and C. Turta, *J. Mater. Chem. C*, 2016, **4**, 5038–5050.
97 C. F. Macrae, I. Sovago, S. J. Cottrell, P. T. A. Galek, P. McCabe, E. Pidcock, M. Platings, G. P. Shields, J. S. Stevens, M. Towler and P. A. Wood, *J. Appl. Crystallogr.*, 2020, **53**, 226–235.